

Local magnetic properties of the antiferromagnetic metal NaV_2O_4 with frustrated double-chain structure investigated by NMR and magnetization measurements

Hikaru Takeda and Masayuki Itoh

Department of Physics, Graduate School of Science, Nagoya University, Furo-cho, Chikusa-ku, Nagoya 464-8602, Japan

Hiroya Sakurai

National Institute for Materials Science, Namiki 1-1, Tsukuba, Ibaraki 305-0044, Japan

(Received 24 July 2012; published 5 November 2012)

We have made NMR and magnetization measurements on a single crystal to investigate local magnetic properties of an antiferromagnetic metal NaV_2O_4 with a frustrated double-chain structure. In the paramagnetic phase, we find there is a double exchange ferromagnetic interaction, which competes with a superexchange antiferromagnetic interaction, yielding a magnetic frustration. In the magnetically ordered state, we propose an incommensurate helical structure with the bc helical plane, which appears due to the competition between the magnetic interactions, as a spin structure. Thus we conclude that the magnetic frustration closely related to a multi-band effect plays an essential role for the magnetic properties of NaV_2O_4 .

DOI: [10.1103/PhysRevB.86.174405](https://doi.org/10.1103/PhysRevB.86.174405)

PACS number(s): 75.25.-j, 75.30.Cr, 75.30.Et, 76.60.-k

I. INTRODUCTION

Multi-orbital systems with strongly correlated electrons have provided intriguing phenomena such as the orbital-selective Mott transition in rutenates,¹ the orbital fluctuations and the electronic nematic order in Fe-based superconductors,² and so on. Then the multi-orbital effects appear with cooperative and/or competing spin and charge degrees of freedom. Also several orbital-dependent electron-electron interactions such as the Hund coupling, Coulomb interactions, and intra- and inter-orbital interactions play important roles for the mechanism of the phenomena. In addition to the orbital effects, a geometrical frustration leads to an anomalous effect on the electron systems.³ One of the most investigated systems with a geometrical frustrated lattice is LiV_2O_4 , where V atoms form the pyrochlore lattice, with heavy electron behavior.⁴⁻⁶ Another is an electron system on a quasi-one-dimensional (quasi-1D) lattice with a frustrated zigzag chain such as hollandite and calcium-ferrite structures.

Recently, in a hollandite-type oxide $\text{K}_2\text{Cr}_8\text{O}_{16}$, which is a ferromagnetic (FM) half metal, a unique metal-insulator transition (MIT) was discovered in the FM phase.⁷⁻⁹ Also $\text{K}_2\text{V}_8\text{O}_{16}$ was found to show an MIT accompanied by the orbital ordering and the spin singlet formation.¹⁰⁻¹³ Mechanisms of the anomalous properties were systematically discussed from density-functional-theory-based electronic structure calculations.¹⁴⁻¹⁶ Another quasi-1D lattice appears in the calcium-ferrite type structure. NaCr_2O_4 was recently found to show a new type of colossal magnetoresistance (CMR),^{17,18} which takes place in the antiferromagnetically ordered phase, different from the conventional CMR in ferromagnetic compounds such as manganites.^{19,20} Also NaV_2O_4 , an antiferromagnetic (AFM) metal, was reported to be a candidate of the quasi-1D system with the multi-orbital and frustration effects.²¹⁻²³ Although physical properties of the calcium-ferrite type oxides strongly depend on the $3d$ orbital states, local electronic states have not been clearly elucidated. Thus an experimental study by means of a microscopic probe such as nuclear magnetic resonance (NMR) is required to clarify the orbital states.⁶

NaV_2O_4 with the mixed valence of $\text{V}^{3+}:\text{V}^{4+}=1:1$ (the average electron number $3d^{1.5}$) crystallizes in the calcium-ferrite type structure (space group $Pnma$) with a V_8O_{16} framework composed of double chains of edge sharing $\text{V}(1)\text{O}_6$ and $\text{V}(2)\text{O}_6$ octahedra as shown in Fig. 1.²¹ Then Na atoms are located in a tunnel of the framework. This oxide exhibits metallic behavior down to 40 mK and shows an AFM transition at $T_N = 140$ K.²¹ Above T_N , the presence of a FM correlation was pointed out in addition to the AFM interactions from the magnetic susceptibility measurement. On the other hand, below T_N , the magnetization measurement on a powdered sample revealed that there are three AFM phases, AFM1–AFM3, in the temperature T versus magnetic field H phase diagram.²² The AFM1 phase appears in a narrow range just below T_N , whereas the AFM3 (AFM2) phase is located below (above) ~ 5.5 T in the T range below the AFM1 phase. Although the complex magnetic properties seem to be related to the interplay of the orbital dependent magnetic properties, local electronic and orbital states which govern them have not been elucidated. Also, spin structures in the AFM phases remain controversial in spite of several experiments such as magnetic susceptibility,²¹ $\mu^+\text{SR}$,^{24,25} and neutron scattering measurements.²⁶

In the present study, we have performed ^{23}Na and ^{51}V NMR measurements to clarify the local electronic states and magnetic properties of NaV_2O_4 . From these measurements on a single crystal, we investigate the anisotropy of the local magnetic properties, which is related to the orbital states of $3d$ electrons at the V sites, and the spin structures in the AFM phases. In the paramagnetic phase, we confirm the presence of the FM correlation and discuss its origin on the basis of the multi-band effect. In the AFM3 phase, we propose an incommensurate helical spin structure, which comes from the competition between the FM and AFM interactions. The phase transition from the AFM3 to AFM2 phases is also discussed.

II. EXPERIMENT PROCEDURE

Single crystals and polycrystalline samples of NaV_2O_4 were prepared as reported in Ref. 22. A single crystal of

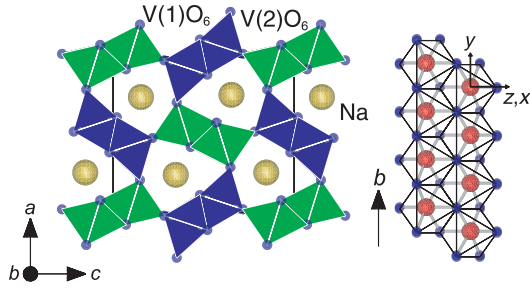


FIG. 1. (Color online) Crystal structure of NaV_2O_4 projected to the ca plane. Also a double chain, the basic unit, in the crystal structure is presented with the local x , y , and z axes.

$0.5 \times 1.0 \times 1.5 \text{ mm}^3$ was used for the present NMR experiment in external magnetic field and the magnetization measurement, whereas the powder sample was used for the NMR measurement under zero external field. NMR measurements were made by using a coherent pulsed spectrometer and a superconducting magnet with a constant field of $H = 3.0$ or 5.8701 T . Fourier-transformed (FT) NMR spectra for spin-echo signals were measured with the sample rotated in the field using a two-axis goniometer. The ^{23}Na and ^{51}V Knight shifts were determined as ${}^\mu K = (v_{\text{res}}^\mu - v_0^\mu)/v_0^\mu$ ($\mu = ^{23}\text{Na}$ and ^{51}V) where v_{res}^μ and v_0^μ ($= 66.114 \text{ MHz}$ for ^{23}Na and 65.704 MHz for ^{51}V) are ^{23}Na and ^{51}V resonance frequencies in NaV_2O_4 and the aqueous NaVO_3 solution, respectively. Frequency-swept ^{51}V NMR spectra at 4.2 K were taken point by point in zero external field. The ^{23}Na (^{51}V) nuclear spin-lattice relaxation rate $1/T_1$ was measured by the inversion recovery method with $H = 5.8701 \text{ T}$ applied to the direction of a magic angle where an electric quadrupole interaction vanishes (the direction of the x axis). Then both ^{23}Na and ^{51}V nuclear magnetizations after an inversion pulse were recovered single-exponentially with T_1 . Magnetic susceptibility and magnetization were measured by using a commercial superconducting quantum interface device (SQUID) magnetometer (Quantum Design, MPMS-XL7).

III. EXPERIMENTAL RESULTS AND DISCUSSION

A. Paramagnetic phase

1. Magnetic susceptibility

Figure 2 shows the T dependence of magnetic susceptibility χ_α ($\alpha = a, b$, and c) measured with $H = 1 \text{ T}$ parallel to the a , b , and c axes in NaV_2O_4 . The present data are also consistent with reported results.^{21,22} Above $T_N = 140 \text{ K}$, χ_α is almost isotropic. Then, as is shown in Fig. 2, average magnetic susceptibility $\chi = \sum_\alpha \chi_\alpha/3$ follows in the T range of 200 – 300 K a relation $\chi = \chi_0 + \frac{C}{T-\Theta}$ with the Curie constant $C = 0.92 \text{ emu}\cdot\text{V}\cdot\text{mol}^{-1}\text{K}^{-1}$, the Weiss temperature $\Theta = 49 \text{ K}$, and $\chi_0 = -1.0 \times 10^{-3} \text{ emu/V}\cdot\text{mol}$ which are dependent on the fitting T range. This means the presence of several magnetic interactions. Below T_N , χ_α is split into parallel and perpendicular susceptibilities due to the AFM order.

2. Knight shift

The angular dependence of the ^{23}Na (a nuclear spin $^{23}I = 3/2$) resonance frequency at 300 K is shown in Fig. 3. In spite

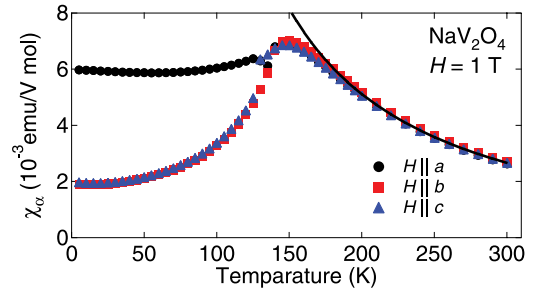


FIG. 2. (Color online) Temperature dependence of magnetic susceptibility χ_α ($\alpha = a, b$, and c) measured with $H = 1 \text{ T}$ applied parallel to the a , b , and c axes, respectively, in NaV_2O_4 . The solid curve represents the fitted result of the average magnetic susceptibility $\chi = \sum_\alpha \chi_\alpha/3$ data to the relation $\chi = \chi_0 + \frac{C}{T-\Theta}$ in the T range of 200 – 300 K .

of one crystallographic Na site, two sets of ^{23}Na NMR spectra with one central and two satellite lines split by the electric quadrupole interaction were observed for H ($= 5.8701 \text{ T}$) in the ca plane, whereas only one set was done for H in the ab and bc planes. This is consistent with the local symmetry at the Na site on a mirror plane perpendicular to the b axis.²⁷

In the first-order perturbation where the electric quadrupole interaction with the electric quadrupole frequency $\nu_Q = \frac{3eQV_{zz}}{2I(2I-1)\hbar}$ with the electric field gradient (EFG) V_{zz} , is much smaller than the Zeeman one, the quadrupole splitting $\delta\nu$ is expressed for H in the bc plane as^{28,29}

$$\delta\nu = \nu_{1a} + \nu_{2a} \cos 2\theta_a + \nu_{3a} \sin 2\theta_a, \quad (1)$$

where θ_a is an angle from the b axis, $\nu_{1a} = \nu_Q(V_{bb} + V_{cc})/V_{zz}$, $\nu_{2a} = \nu_Q(V_{bb} - V_{cc})/V_{zz}$, and $\nu_{3a} = -2\nu_Q V_{bc}/V_{zz}$ with the EFG tensor $V_{\alpha\beta}$ ($\alpha, \beta = a, b, c$). Similar relations for H rotations in the ab and ca planes are obtained by cyclic permutation. After determining the EFG tensor components in the abc coordinate system with Eq. (1), we can obtain x , y , and z principal components and principal axes by diagonalizing the EFG tensor. Also we can determine ν_Q and the asymmetry

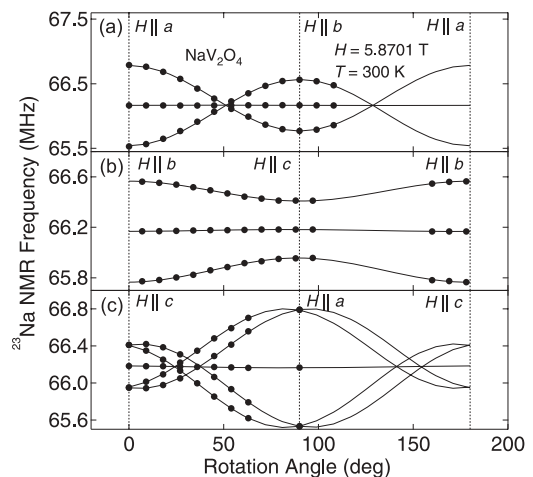


FIG. 3. Angular dependence of the ^{23}Na NMR frequency at 300 K with $H = 5.8701 \text{ T}$ rotated in the (a) ab , (b) bc , and (c) ca planes of NaV_2O_4 . The solid curves are the fitted results of the data to Eqs. (1) and (2) in the text.

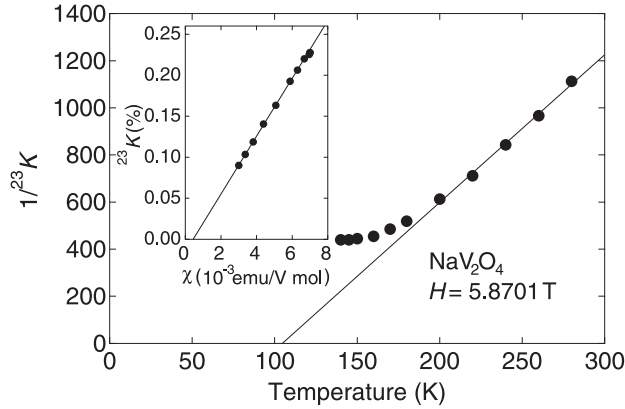


FIG. 4. Temperature dependence of the ^{23}Na Knight shift with $H = 5.8701$ T applied to the magic angle, $\theta_c \sim 52^\circ$, in the ab plane of NaV_2O_4 . The solid line is the fitted result of the data to the Curie-Weiss law $1/^{23}K = (T - \Theta)/C$. The inset shows the ^{23}K versus magnetic susceptibility plots.

parameter of EFG $\eta = |V_{xx} - V_{yy}|/|V_{zz}|$ ($|V_{xx}| \leq |V_{yy}| \leq |V_{zz}|$). The observed angular dependence of the NMR frequency can be well fitted to Eq. (1) with $\nu_Q = 0.64$ MHz and $\eta = 0.25$ as seen in Fig. 3. Then the z (y) axis is located at $\theta_b = \pm 84^\circ$ ($\theta_a = 0^\circ$). A fact that the b axis is a principal one is consistent with the Na site symmetry.

On the other hand, the Knight shift K in the abc coordinate system is expressed as^{29,30}

$$K = k_{1a} + k_{2a} \cos 2\theta_a + k_{3a} \sin 2\theta_a, \quad (2)$$

where $k_{1a} = (K_{bb} + K_{cc})/2$, $k_{2a} = (K_{bb} - K_{cc})/2$, and $k_{3a} = K_{bc}$ with K tensor components $K_{\alpha\beta}$, when H is applied in the bc plane. Similar relations for H rotations in the ab and ca planes are obtained by cyclic permutation. Principal components of the tensor $(K_x, K_y, K_z) = (K_k)$ and also principal axes can be obtained by diagonalizing it.

After subtracting the second-order quadrupole effect from the resonance frequency of the ^{23}Na central line at 300 K, we fitted the experimental data of the ^{23}Na Knight shift to Eq. (2) and obtained the almost isotropic shift $^{23}K \sim 0.086$ % with small extrinsic anisotropic ones which are almost ascribed to the cancellation between dipole and demagnetization fields in the present single crystal. Thus the T dependence of ^{23}K was measured with H applied to the magic angle, $\theta_c \sim 52^\circ$, in the ab plane, and the result is presented in Fig. 4. Then $1/^{23}K$ above ~ 200 K obeys the Curie Weiss (CW) law $1/^{23}K = (T - \Theta)/C$ with $C = 0.159$ K and $\Theta = 105$ K, indicating the presence of the ferromagnetic correlation. Below ~ 200 K, ^{23}K deviates from the CW law toward T_N . The isotropic shift is ascribed to a transferred hyperfine field with a coupling constant ^{23}A , which is obtained as 1.96 kOe/ μ_B from the ^{23}K versus χ plots in the inset of Fig. 4, coming from the nine neighboring V sites.

In order to determine the ^{51}V Knight shift ^{51}K , we performed ^{51}V NMR measurements on the single crystal with $H = 5.8701$ T rotated in the ab , bc , and ca planes. The electric quadrupole splitting was not observed because of small EFGs at the V sites as seen in the inset of Fig. 5. The anisotropy of the nuclear spin-spin relaxation time T_2 prevented us from observing the spectra in all the angle range. As is seen in

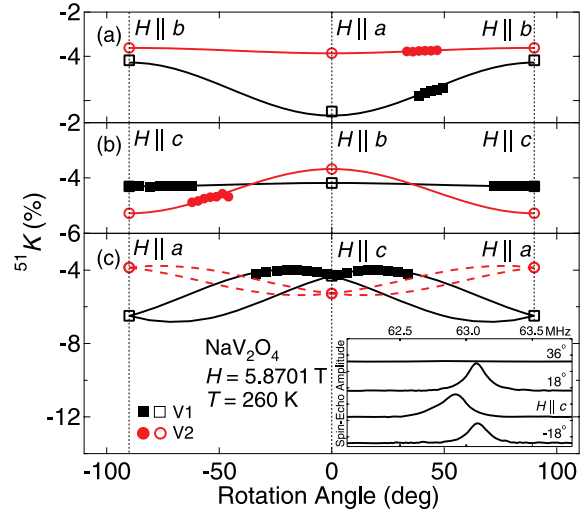


FIG. 5. (Color online) Angular dependence of the ^{51}V Knight shift at 260 K with H rotated in the (a) ab , (b) bc , and (c) ca planes of NaV_2O_4 . The solid and dashed curves are the fitted results of the data to Eq. (2) in the text and the curves calculated from the fitted results, respectively. The solid symbols represent the experimental data, whereas the open ones denote the $^{51}K_a$, $^{51}K_b$, and $^{51}K_c$ results calculated from the fitted curves. The inset shows ^{51}V NMR spectra at 260 K with $H = 5.8701$ T rotated in the ca plane.

Fig. 5 which shows the angular dependence of ^{51}K at 260 K, two (four) sets of NMR spectra were observed for H in the ab and bc (ca) planes due to the local symmetry at the V1 and V2 sites on the mirror plane with the b axis, whereas only two sets from the V1 site could be observed due to the short T_2 for H in the ca plane. The observed angular dependence of ^{51}K is well fitted to Eq. (2). We obtained $^{51}K_k$ values for the V1 and V2 sites as $(^{51}K_k) = (-4.0, -4.3, -6.9)\%$ and $(-3.7, -3.8, -5.4)\%$ respectively. The z axis, which is located at $\theta_b = 71^\circ$ (14°) for V1 (V2) in the ca plain, is almost parallel to the apical direction of the VO_6 octahedron, and the y axis is parallel to the b axis as presented in Fig. 1. Also we determined the ^{51}K tensors at 180, 220, and 295 K. The T dependence of $^{51}K_k$ ($k = x, y, \text{ and } z$) is presented with average magnetic susceptibility $\chi = \sum_{\alpha} \chi_{\alpha}/3$ in Fig. 6. The ^{51}V Knight shifts show the almost axial anisotropy and the CW-like behavior as seen in Fig. 6.

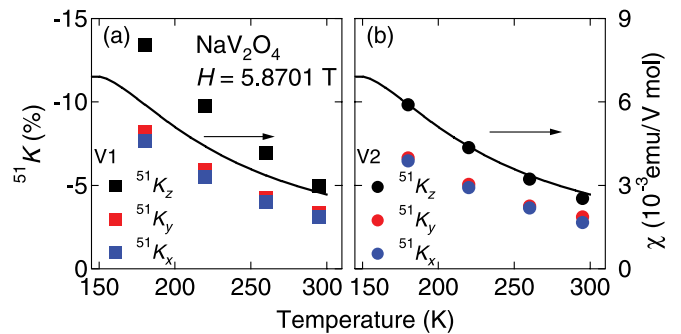


FIG. 6. (Color online) Temperature dependence of the ^{51}V Knight shift components $^{51}K_x$, $^{51}K_y$, and $^{51}K_z$ for the (a) V1 and (b) V2 sites in NaV_2O_4 . The solid curves represent average magnetic susceptibility of NaV_2O_4 .

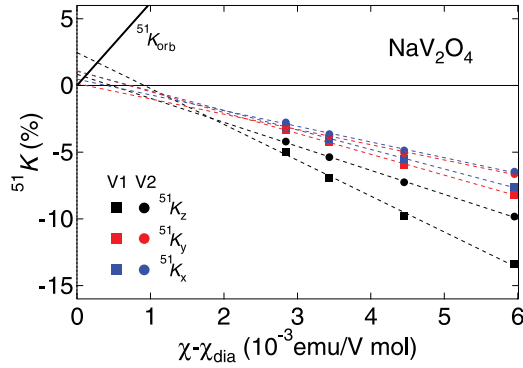


FIG. 7. (Color online) ^{51}V Knight shift versus magnetic susceptibility plots for the V1 and V2 sites in NaV_2O_4 . The $^{51}K_x$, $^{51}K_y$, and $^{51}K_z$ represent the principal components of the ^{51}K tensor. The dashed lines are the fitted results of the data to $^{51}K = K_0 + \frac{^{51}A_{\text{spin}}}{N_A\mu_B}\chi$, whereas the solid line represents $^{51}K_{\text{orb}} = \frac{^{51}A_{\text{orb}}}{N_A\mu_B}\chi_{\text{orb}}$.

3. Hyperfine tensor

First we will determine the hyperfine tensor, which is useful to study the electronic structure in multi-orbital systems, from a conventional analysis of K and χ data. In vanadium oxides, ^{51}K is decomposed into spin and orbital parts as $^{51}K = ^{51}K_{\text{spin}} + ^{51}K_{\text{orb}}$. Also χ is the sum of spin, orbital, and diamagnetic susceptibilities, $\chi = \chi_{\text{spin}} + \chi_{\text{orb}} + \chi_{\text{dia}}$, where χ_{dia} is evaluated as -3.5×10^{-5} emu/V-mol for NaV_2O_4 .³¹ Then $^{51}K_p$ ($p = \text{spin and orb}$) is expressed as $^{51}K_p = \frac{^{51}A_p}{N_A\mu_B}\chi_p$ where $^{51}A_{\text{spin}}$ is the spin hyperfine coupling constant, $^{51}A_{\text{orb}}$ is the orbital one due to the Van Vleck process, N_A is the Avogadro's number, and μ_B is the Bohr magneton. Figure 7 shows the ^{51}K versus χ plots, where χ is the average magnetic susceptibility, with T as an implicit parameter for the V1 and V2 sites. Using a value of $^{51}A_{\text{orb}} = 2\mu_B\langle r^{-3} \rangle = 346$ kOe/ μ_B , which is calculated from an expectation value of r^{-3} for the V $3d$ orbital $\langle r^{-3} \rangle (=r_{\text{mag}}\langle r^{-3} \rangle_{\text{HF}}$ with a reduction factor $r_{\text{mag}} = 0.8$ in a metallic system³² and an average free-ion value of $\langle r^{-3} \rangle$, $\langle r^{-3} \rangle_{\text{HF}}$, evaluated from 3.21 a.u.³³ for V^{4+} and 3.68 a.u. for V^{3+}), we obtain from the ^{51}K versus χ plots the values of $^{51}K_{\text{orb}}$ and χ_{orb} for V1 and V2 as listed in Table I. These values show the nearly axial symmetry with the local symmetry z axis. The slopes of the ^{51}K versus χ plots yield the values of $^{51}A_{\text{spin}}$ for V1 and V2 as listed in Table II. It should be noted that $^{51}A_{\text{spin}}$ has the nearly axial symmetry with the z axis, which is consistent with the orbital susceptibility. Also the isotropic hyperfine coupling constant $^{51}A_{\text{iso}} = \sum_k ^{51}A_{\text{spin}}^k/3$ is -106 (-77) kOe/ μ_B for V1 (V2). These values are reasonable compared with -85 in VO_2 ($3d^1$)³⁴ and -140 kOe/ μ_B in V_2O_3 ($3d^2$).³⁵ The anisotropic components of the $^{51}A_{\text{spin}}$ tensor

TABLE I. Orbital ^{51}V Knight shifts $^{51}K_{\text{orb}}^k$ ($k = x, y, \text{ and } z$) and magnetic susceptibilities χ_{orb}^k for the V1 and V2 sites in NaV_2O_4 . The values of χ_{orb}^k are presented in the unit of 10^{-4} emu/V-mol.

| Site | K_{orb}^x (%) | K_{orb}^y (%) | K_{orb}^z (%) | χ_{orb}^x | χ_{orb}^y | χ_{orb}^z |
|------|------------------------|------------------------|------------------------|-----------------------|-----------------------|-----------------------|
| V1 | 0.88 | 0.86 | 1.7 | 1.4 | 1.4 | 2.7 |
| V2 | 0.39 | 0.12 | 0.65 | 0.6 | 0.2 | 1.0 |

TABLE II. Spin hyperfine coupling constants $^{51}A_{\text{spin}}^k$ ($k = x, y, \text{ and } z$) and anisotropic components of the $^{51}A_{\text{spin}}$ tensor $^{51}A_{\text{aniso}}^k$ for the V1 and V2 sites in NaV_2O_4 . The values are presented in the unit of kOe/ μ_B .

| Site | $^{51}A_{\text{spin}}^x$ | $^{51}A_{\text{spin}}^y$ | $^{51}A_{\text{spin}}^z$ | $^{51}A_{\text{aniso}}^x$ | $^{51}A_{\text{aniso}}^y$ | $^{51}A_{\text{aniso}}^z$ |
|------|--------------------------|--------------------------|--------------------------|---------------------------|---------------------------|---------------------------|
| V1 | -81 | -87 | -150 | 25 | 19 | -44 |
| V2 | -66 | -64 | -100 | 11 | 13 | -23 |

$^{51}A_{\text{aniso}}^k = ^{51}A_{\text{spin}}^k - ^{51}A_{\text{iso}}$ ($k = x, y, \text{ and } z$) for V1 and V2 are obtained as listed in Table II.

Based on the hyperfine tensors obtained above, we discuss the electronic structure of NaV_2O_4 . When the orbital and spin-orbit hyperfine interactions are neglected as discussed in other vanadium oxides,^{12,36,37} the magnetic hyperfine interaction \mathcal{H} is expressed as

$$\mathcal{H} = \sum_i 2\mu_B\gamma_n\hbar\mathbf{I} \cdot ^{51}\mathbf{A}_i \cdot \mathbf{s}_i, \quad (3)$$

where γ_n is the nuclear gyromagnetic ratio, \hbar is the Plank's constant, \mathbf{I} is the nuclear spin operator, and \mathbf{s}_i is the i th electron spin. Also the hyperfine coupling tensor $^{51}\mathbf{A}_i$ is written by $^{51}\mathbf{A}_i = -(\kappa\mathbf{1} + \frac{\kappa}{21}\mathbf{q}_i)\langle r^{-3} \rangle$ where κ is a parameter of the Fermi contact interaction due to the core-polarization effect, and \mathbf{q}_i is the electron quadrupole moment tensor $q_{\alpha\beta} = \frac{3}{2}(l_{\alpha}l_{\beta} + l_{\beta}l_{\alpha}) - \delta_{\alpha\beta}l^2$ with the orbital momentum l .^{33,38} Then the first term in $^{51}\mathbf{A}_i$ is isotropic, whereas the second yields the anisotropic tensor which provides useful information on an electron number of each orbital in the multi-orbital systems.

In the present t_{2g} system, χ is decomposed of magnetic susceptibility of each t_{2g} orbital as $\chi = \sum_j f_j\chi_j$ where f_j ($j = x^2 - y^2, yz, \text{ and } zx$) is a fraction of the d_j orbital. Then the anisotropic hyperfine coupling constant $^{51}A_{\text{aniso}}^k$ ($k = x, y, \text{ and } z$) is expressed as^{6,12}

$$^{51}A_{\text{aniso}}^k = -\frac{2}{21}\langle r^{-3} \rangle \sum_j f_j q_j^k, \quad (4)$$

where $(q_{yz}^k) = 3(2, -1, -1)$, $(q_{zx}^k) = 3(-1, 2, -1)$, and $(q_{x^2-y^2}^k) = 3(-1, -1, 2)$. The approximately axial anisotropy observed for ^{51}K in NaV_2O_4 reasonably leads to an assumption $f_{yz} \sim f_{zx}$. Then, comparing Eq. (4) with the experimental data, we obtain $(f_{x^2-y^2}, f_{yz}, f_{zx}) \sim (0.6, 0.2, 0.2)$ for V1 and $\sim (0.5, 0.25, 0.25)$ for V2. These results may correspond to electron occupation numbers, $(d_{x^2-y^2}^{0.9}, d_{yz}^{0.3}, d_{zx}^{0.3})$ for V1 and $(d_{x^2-y^2}^{0.75}, d_{yz}^{0.375}, d_{zx}^{0.375})$ for V2, although the bandwidth and/or the electron correlation prevent us from knowing the precise numbers via the local magnetic susceptibilities. Thus the 1.5 $3d$ electrons predominantly occupy the $d_{x^2-y^2}$ orbital rather than d_{yz} and d_{zx} . This result indicates that $d_{x^2-y^2}$ has a lower energy than those of the other orbitals, d_{yz} and d_{zx} , as schematically presented in Fig. 8(a).

The electronic structure mentioned above is consistent with the result in the first-principle electronic calculation by Sakamaki *et al.* for the half-metallic ferromagnet $\text{K}_2\text{Cr}_8\text{O}_{16}$ ($3d^{2.25}$) with the hollandite structure having zigzag chains similar to those in NaV_2O_4 .¹⁵ They found a rather dispersionless narrow band predominantly composed of $d_{x^2-y^2}$

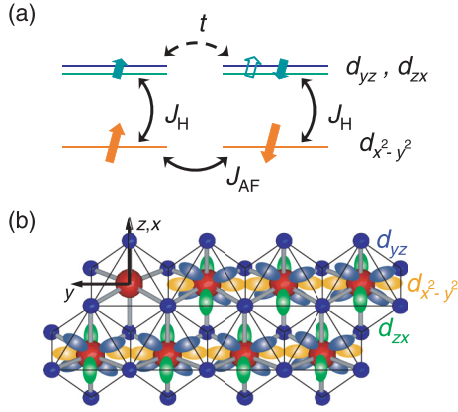


FIG. 8. (Color online) (a) Schematic energy levels of t_{2g} orbitals in NaV_2O_4 . J_H , J_{AF} , and t represent the onsite Hund coupling, the offsite antiferromagnetic interaction, and the transfer integral, respectively. (b) Three t_{2g} orbitals on a double chain in NaV_2O_4 . The x , y , and z axes in the local coordinate system are also presented.

and dispersive bands having the d_{zx} and d_{yz} character with strong admixture of the oxygen $2p$ orbital and proposed a double exchange mechanism responsible to ferromagnetism of $\text{K}_2\text{Cr}_8\text{O}_{16}$. This theoretical model is applicable to NaV_2O_4 with a localized electron in the $d_{x^2-y^2}$ orbital and itinerant ones in d_{yz} and d_{zx} . This electron configuration results in the double exchange process yielding the FM correlation observed in the paramagnetic phase. In addition to the double exchange, the AFM interaction is expected to exist due to a direct $d_{x^2-y^2}$ - $d_{x^2-y^2}$ path along the double-chain direction as seen in Fig. 8(b). Consequently there should be the competition between the FM interaction along a rung and the AFM one along a leg. Thus this magnetic frustration is expected to affect the magnetic properties, the spin structure, and the phase diagram in the magnetically ordered phases of NaV_2O_4 . Also the competition between the FM and AFM interactions is dependent on the electron number in the double-chain systems. That is, the FM interaction overcomes the AFM one in $\text{K}_2\text{Cr}_8\text{O}_{16}$ ($3d^{2.25}$), leading to the half-metallic ferromagnetism, whereas the FM behavior does not appear in $\text{K}_2\text{V}_8\text{O}_{16}$ ($3d^{1.25}$) with the predominant AFM interaction.

4. Nuclear spin-lattice relaxation rate

To clarify the magnetic correlation in the paramagnetic phase of NaV_2O_4 , we measured the T dependence of the ^{51}V (^{23}Na) nuclear spin-lattice relaxation rate $1/T_1$ with $H \parallel x$ (at the magic angle, $\theta_c = 52^\circ$), in the ab plane for the V1 (Na) site. As seen in Fig. 9(a), $1/T_1 T$, which is proportional to $\Sigma_{\mathbf{q}} \text{Im} \chi_{\perp}(\mathbf{q}, \omega_n)$ where $\chi_{\perp}(\mathbf{q}, \omega_n)$ is the transverse dynamical susceptibility with the wave vector \mathbf{q} and the nuclear Larmor frequency ω_n , does not obey the Korringa relation, $1/T_1 T = \text{constant}$, which appears in Fermi liquid systems. This indicates the presence of the strong electron correlation in the present system. Then the T dependence can be fitted to the CW law, $1/T_1 T = C/(T - \Theta)$ with $C = 3.3 \times 10^4$ (11) s^{-1} and $\Theta = 98$ (100) K, for the V1 (Na) site in the T range of 200–300 K. Thus these CW behaviors indicate that $1/T_1 T$ of both V and Na may be scaled to the Knight shifts. Figure 9(b) shows the $1/T_1 T |K_{\perp}|$ versus T plots for the Na and V1 sites

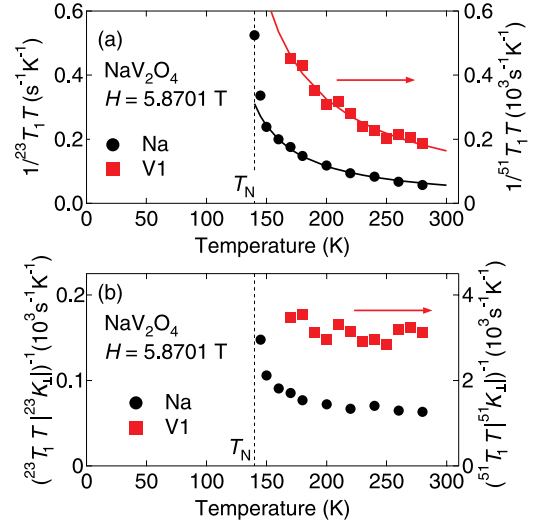


FIG. 9. (Color online) Temperature dependence of (a) $1/T_1 T$ and (b) $1/T_1 T |K_{\perp}|$ for ^{23}Na and ^{51}V nuclei with $H = 5.8701$ T applied to the magic angle and parallel to the x axis, respectively, in NaV_2O_4 . The solid curves are the fitted results of the data to the Curie-Weiss law.

in NaV_2O_4 . In the plots, K_{\perp} is the Knight shift perpendicular to H defined as $^{51}K_{\perp} = (^{51}K_y - ^{51}K_{\text{orb}}^y + ^{51}K_z - ^{51}K_{\text{orb}}^z)/2$ to discuss spin fluctuations at the V1 site, whereas $^{23}K_{\perp} = ^{23}K$ for Na. As seen in Fig. 9(b), the $1/T_1 T |K_{\perp}|$, which is approximately proportional to $\Sigma_{\mathbf{q}} \text{Im} \chi_{\perp}(\mathbf{q}, \omega_n)/\chi_{\perp}(0, \omega_n)$, versus T is almost T -independent above ~ 200 K, whereas $1/T_1 T |K_{\perp}|$ below ~ 200 K gradually increases due to the growth of the AFM fluctuation. In particular, $1/T_1 T |K_{\perp}|$ of ^{23}Na monitors the critical slowing down which divergently enhances $1/T_1 T$ towards T_N . Thus, the present results indicate that the AFM spin fluctuation overcomes below ~ 200 K the FM one predominant at high temperatures. From the dynamical point of view, this also supports the model of the intra- and inter-orbital interactions presented in Fig. 8(a).

B. Magnetically ordered phase

Below T_N , three antiferromagnetic phases, AFM1–AFM3, have been reported to exist in the T - H phase diagram from magnetic susceptibility measurements.²² The AFM1 phase is located in the small region just below T_N , whereas the AFM2 (AFM3) phase appears above (below) ~ 5.5 T. Although several models for the spin structure in the AFM phases have been proposed from magnetization,²¹ μ^+ SR,^{24,25} and neutron scattering measurements,²⁶ the spin structure remains controversial. We present experimental results of magnetization and NMR, and discuss the spin structure and the magnetic phase transition in a magnetic field.

1. Magnetization curve

As seen in Fig. 2, below T_N , $\chi_b \sim \chi_c < \chi_a$, indicating that the easy axis of the magnetic moments in the AFM3 phase is perpendicular to the a axis. This is in contrast to $\chi_b < \chi_c \sim \chi_a$ measured at 5 T.²¹ Magnetization curves $M_{\alpha}(H)$ ($\alpha = a, b$, and c) for $H \parallel a$ at 5 K are presented in Fig. 10. Both $M_a(H)$ and $M_b(H)$ linearly increase with increasing H in the observed

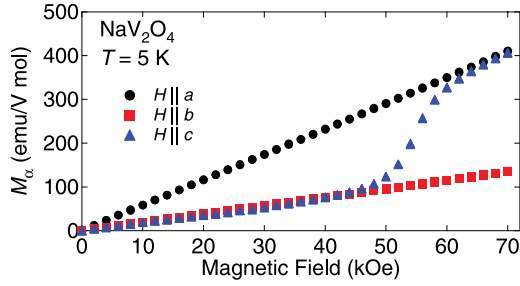


FIG. 10. (Color online) Magnetization curve $M_\alpha(H)$ for $H \parallel \alpha$ ($\alpha = a, b,$ and c) at 5 K in NaV_2O_4

H range, whereas $M_c(H)$ traces $M_b(H)$ below 5 T, gradually jumps in the H range of 5 T $< H < 6$ T, and again traces $M_a(H)$ above 6 T. These results of magnetic susceptibility and magnetization measurements clearly show a magnetic phase transition takes place from the AFM3 to AFM2 phases at ~ 5.5 T for $H \parallel c$ at 5 K.

2. NMR spectrum and spin structure

^{23}Na NMR measurements are useful to determine the spin structure of NaV_2O_4 . The inset of Fig. 11 shows typical ^{23}Na NMR spectra with $H = 5.8701$ T applied to the b axis above and below T_N . The spectrum above T_N has one central and two satellite lines split by the electric quadrupole interaction, whereas each line becomes a broad spectrum with two peaks below T_N . The characteristic broad spectrum shows a distribution of an internal field \mathbf{H}_n , governed by the spin structure, at the Na sites. Also the difference between the NMR frequencies at the double peaks of the center line, $\Delta\nu_{\text{res}}$, denoted by the red arrows in the inset follows the T dependence of the magnetic moments. Figure 12 shows the angular dependence of $\Delta\nu_{\text{res}}$ with $H = 3.0$ T rotated in the ab and bc planes at 20 K. $\Delta\nu_{\text{res}} \neq 0$ for the bc rotation, while $\Delta\nu_{\text{res}} \sim 0$ for $H \parallel a$, indicating the magnetic moments in the bc plane.

In the magnetically ordered phases of NaV_2O_4 , the ^{23}Na NMR frequency ν_{res} is expressed as $\nu_{\text{res}} = 2\pi\gamma_n |\mathbf{H}_0 + \mathbf{H}_n|$ where \mathbf{H}_n is composed of the dipole field from the V magnetic moments \mathbf{H}_{dip} and the transferred hyperfine field from the nine neighboring V sites \mathbf{H}_{tr} with an isotropic coupling constant

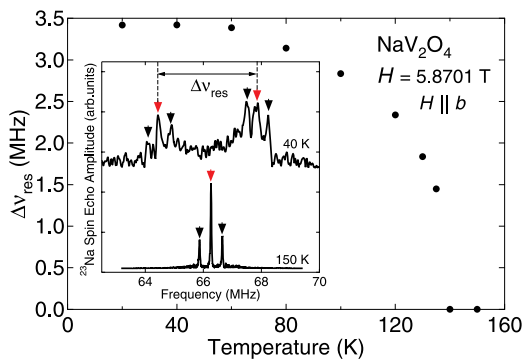


FIG. 11. (Color online) Temperature dependence of the difference between the NMR frequencies, where ^{23}Na spectrum with $H (=5.8701$ T) $\parallel b$ shows the double peaks, $\Delta\nu_{\text{res}}$ in NaV_2O_4 . The inset shows typical ^{23}Na NMR spectra above and below T_N .

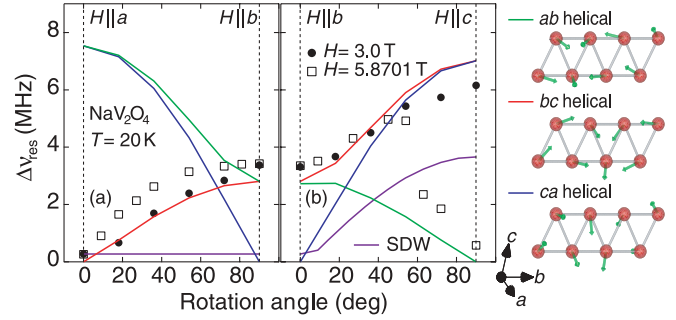


FIG. 12. (Color online) Angular dependence of $\Delta\nu_{\text{res}}$ at 20 K with $H = 3.0$ and 5.8701 T rotated in the (a) ab and (b) bc planes of NaV_2O_4 . The solid curves are the calculated results, assuming spin structure models, i.e., the incommensurate helical structures with the helical $ab, bc,$ or ca plane, and the incommensurate spin density wave (SDW) with the spin moments parallel to the c axis.

$^{23}A_{\text{tr}} = ^{23}A/9 = 218 \text{ Oe}/\mu_B$ evaluated from the $K-\chi$ analysis in the paramagnetic phase. Here it should be noted that the demagnetization and Lorentz fields are negligibly small compared with H_{dip} and H_{tr} in the magnetically ordered phase.

Up to now, several models have been proposed as a spin structure at 0 T in the AFM3 phase such as antiferromagnetically coupled ferromagnetic chains,²¹ the collinear AFM order,²⁴ the incommensurate spin-density wave (SDW),²⁶ and the helical order.²⁵ We analyze the ^{23}Na NMR results based on these models. Among the models, the collinear AFM models cannot reproduce the observed broad NMR spectrum which strongly indicates an incommensurate spin structure. This is consistent with the observation of the incommensurate \mathbf{q} vector, $\mathbf{q}_0 = 2\pi(0, 0.191, 0)$, in the neutron scattering experiment.²⁶ Thus we should look for SDW and helical spin structures. Assuming the SDW model²⁶ with the magnetic moments \mathbf{m} expressed as $\mathbf{m} = m_0[0, 0, \sin(\mathbf{q}_0 \cdot \mathbf{r}/b)]$ with $m_0 = 0.77\mu_B$ and the lattice constant b , and the helical structure models as expressed by, for instance, $\mathbf{m} = m_0[0, \cos(\mathbf{q}_0 \cdot \mathbf{r}/b), \sin(\mathbf{q}_0 \cdot \mathbf{r}/b)]$ with $m_0 = 1.1\mu_B$ for the model on the helical bc plane, we calculate the angular dependence of $\Delta\nu_{\text{res}}$ at the Na sites. Comparing these calculated results with the experimental data at 3 T in the AFM3 phase, only the helical structure in the bc plane can well reproduce the experimental result as seen in Fig. 12. The rejection of the SDW model is supported by a fact that we could not detect the resonance frequency dependence of $1/T_1$ which is expected to appear in SDW phases.³⁹ Also the helical model can approximately reproduce the ^{51}V NMR spectrum, where a correction due to the T_2 process is made, at 0 T and 4.2 K as shown in Fig. 13. The NMR spectrum is governed by the dipole field and the hyperfine field with the hyperfine tensor $^{51}\mathbf{A}$, which is determined by the $K-\chi$ plots in the paramagnetic state. The dashed (dotted) curve in Fig. 13 is calculated for the helical model on the bc plain (the plain with the rotated angle of 9° around the c axis, for comparison) with $m_0 = 1.35\mu_B$ and $\mathbf{q}_0 = 2\pi(0, 0.191, 0)$. Then the calculated NMR spectra are convoluted by a Gaussian with full width at half maximum of 4.0 MHz. These spectra almost reproduce the observed NMR spectrum except the slight deviation which might come from the inter-chain configuration of the magnetic moments and the small difference between the moments at the two V sites.

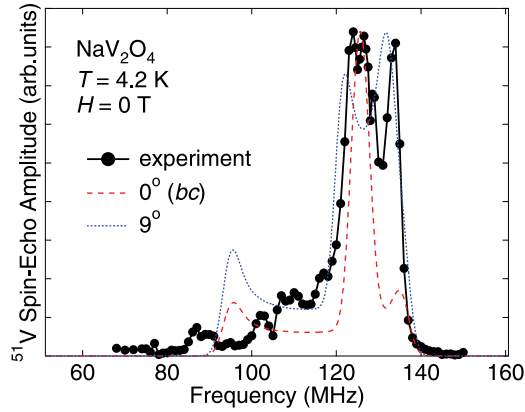


FIG. 13. (Color online) ^{51}V NMR spectrum of NaV_2O_4 under zero external field at 4.2 K. The dashed (dotted) curve represents the NMR spectrum calculated for the incommensurate helical spin structure on the bc plain (the plain with the rotated angle of 9° around the c axis), whereas the solid curve is guide to the eye.

Thus, from the analysis of both the ^{23}Na and ^{51}V NMR spectra mentioned above, we propose the incommensurate helical spin structure on the bc plain in the AFM3 phase of NaV_2O_4 .

We discuss the phase transition from the AFM3 to AFM2 phases in a magnetic field. The change in $M_c(H)$ at ~ 5.5 T is considered to take place due to the flop of the spin moments from the bc to ab planes. This behavior was also observed in the NMR experiment, namely, a sudden change occurs at $\theta_a \sim 55^\circ$, where the c component of H reaches a critical field for the spin flop, in the angular dependence of $\Delta\nu_{\text{res}}$ at $T = 20$ K with $H = 5.8701$ T rotated in the bc plane as seen in Fig. 12(b). These magnetization and NMR experimental results clearly show that the helical plane flops from the bc to ab planes at ~ 5.5 T, when H is applied to the c axis at 5 K. Thus, we propose the arrangement of the magnetic moments in H as schematically shown in Fig. 14.

This helical spin order is ascribed to the competition of the FM and AFM interactions. In a double-chain spin system with the nearest FM and second nearest AFM exchange couplings, J_1 and J_2 , respectively, a helical spin order appears for the ratio $|J_1/J_2| > 1/4$.⁴⁰ Indeed, the helical spin order was observed in quantum spin systems ($S = 1/2$) with frustrated chains such as LiCuO_2 and LiCuVO_4 .^{41–44} Although NaV_2O_4 is an itinerant system, the configuration of the magnetic interactions may have the similar situation and result in the helical spin order. Inelastic neutron scattering measurements of the spin excitation spectrum are desired to obtain the J_1 and J_2 values in NaV_2O_4 .

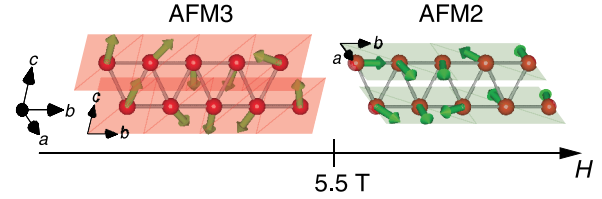


FIG. 14. (Color online) Schematic spin structures in the AFM3 (below ~ 5.5 T) and AFM2 (above ~ 5.5 T) phases of NaV_2O_4 . The light red and green planes represent the bc and ab ones, respectively, where the helical spin moments are located.

IV. CONCLUSION

We have performed ^{23}Na and ^{51}V NMR measurements to clarify the local magnetic properties of the antiferromagnetic metal NaV_2O_4 with the calcium ferrite structure. In the paramagnetic phase, we confirmed the presence of the ferromagnetic correlation. Also, from the analysis of the anisotropic ^{51}V Knight shift, we clarified the orbital state leading to the ferromagnetic interaction, which is due to the double exchange mechanism, along the rung of the double chain. Also the antiferromagnetic interaction due to the direct $d-d$ path along the chain direction was pointed out to compete with the ferromagnetic one, resulting in the magnetic frustration. Below $T_N = 140$ K, the helical magnetic structure was found to appear in the AFM3 phase due to the magnetic competition. Then the helical plane flops at ~ 5.5 T from the bc to ab planes, when the external field is applied to the c axis.

ACKNOWLEDGMENTS

The authors would like to thank Y. Shimizu, Y. Ohta, Y. Kobayashi, and M. Sato for fruitful discussion, and S. Inoue for technical assistance. This study was financially supported by the Grant-in-Aid for Scientific Research on Priority Area “Novel State of Matter Induced by Frustration” (Grant No. 22014006) from the Ministry of Education, Culture, Sports, Science, and Technology of Japan, and the Grants-in-Aid for Scientific Research (Grant Nos. 22246083 and 24340080) and the “Funding Program for World-Leading Innovative R&D on Science and Technology (FIRST Program)” from the Japan Society for the Promotion of Science (JSPS). One of the authors, H.T., was also supported by the Program for Leading Graduate Schools entitled “Integrative Graduate Education and Research Program in Green Natural Sciences” and the Grant-in-Aid for JSPS Fellows.

¹V. I. Anisimov, I. A. Nekrasov, D. E. Kondakov, T. M. Rice, and M. Sgrist, *Eur. Phys. J. B* **25**, 191 (2002).

²H. Kontani, Y. Inoue, T. Saito, Y. Yamakawa, and S. Onari, *Solid State Commun.* **152**, 718 (2012).

³C. Lacroix, *J. Phys. Soc. Jpn.* **79**, 011008 (2010), and references therein.

⁴S. Kondo, D. C. Johnston, C. A. Swenson, F. Borsa, A. V. Mahajan, L. L. Miller, T. Gu, A. I. Goldman, M. B. Maple, D. A. Gajewski,

E. J. Freeman, N. R. Dilley, R. P. Dickey, J. Merrin, K. Kojima, G. M. Luke, Y. J. Uemura, O. Chmaissem, and J. D. Jorgensen, *Phys. Rev. Lett.* **78**, 3729 (1997).

⁵C. Urano, M. Nohara, S. Kondo, F. Sakai, H. Takagi, T. Shiraki, and T. Okubo, *Phys. Rev. Lett.* **85**, 1052 (2000).

⁶Y. Shimizu, H. Takeda, M. Tanaka, M. Itoh, S. Niitaka, and H. Takagi, *Nature Commun.* **3**, 981 (2012).

- ⁷K. Hasegawa, M. Isobe, T. Yamauchi, H. Ueda, J. I. Yamaura, H. Gotou, T. Yagi, H. Sato, and Y. Ueda, *Phys. Rev. Lett.* **103**, 146403 (2009).
- ⁸A. Nakao, Y. Yamaki, H. Nakao, Y. Murakami, K. Hasegawa, M. Isobe, and Y. Ueda, *J. Phys. Soc. Jpn.* **81**, 954710 (2012).
- ⁹J. Sugiyama, H. Nozaki, M. Mansson, K. Prsa, D. Andreica, A. Amato, M. Isobe, and Y. Ueda, *Phys. Rev. B* **85**, 214407 (2012).
- ¹⁰M. Isobe, S. Koishi, N. Kouno, J. Yamaura, T. Yamauchi, H. Ueda, H. Gotou, T. Yagi, and Y. Ueda, *J. Phys. Soc. Jpn.* **75**, 073801 (2006).
- ¹¹M. Isobe, S. Koishi, S. Yamazaki, J. Yamaura, H. Gotou, T. Yagi, and Y. Ueda, *J. Phys. Soc. Jpn.* **78**, 114713 (2009).
- ¹²Y. Shimizu, K. Okai, M. Itoh, M. Isobe, J.-I. Yamaura, T. Yamauchi, and Y. Ueda, *Phys. Rev. B* **83**, 155111 (2011).
- ¹³A. C. Komarek, M. Isobe, J. Hemberger, D. Meier, T. Lorenz, D. Trots, A. Cervellino, M. T. Fernandez-Diaz, Y. Ueda, and M. Braden, *Phys. Rev. Lett.* **107**, 027201 (2011).
- ¹⁴M. Sakamaki, S. Horiuchi, T. Konishi, and Y. Ohta, arXiv:0811.4338.
- ¹⁵M. Sakamaki, T. Konishi, and Y. Ohta, *Phys. Rev. B* **80**, 024416 (2009).
- ¹⁶T. Toriyama, A. Nakao, Y. Yamaki, H. Nakao, Y. Murakami, K. Hasegawa, M. Isobe, Y. Ueda, A. V. Ushakov, D. I. Khomskii, S. V. Streltsov, T. Konishi, and Y. Ohta, *Phys. Rev. Lett.* **107**, 266402 (2011).
- ¹⁷H. Sakurai, T. Kolodiazny, Y. Mihiue, E. Takayama-Muromachi, Y. Tanabe, and H. Kikuchi, *Angew. Chem. Int. Ed.* **51**, 6653 (2012).
- ¹⁸H. Takeda, Y. Shimizu, M. Itoh, H. Sakurai, and E. Takayama-Muromachi (unpublished).
- ¹⁹A. Urushibara, Y. Moritomo, T. Arima, A. Asamitsu, G. Kido, and Y. Tokura, *Phys. Rev. B* **51**, 14103 (1995).
- ²⁰E. Dagotto, T. Hotta, and A. Moreo, *Phys. Rep.* **344**, 1 (2001).
- ²¹K. Yamaura, M. Arai, A. Sato, A. B. Karki, D. P. Young, R. Movshovich, S. Okamoto, D. Mandrus, and E. Takayama-Muromachi, *Phys. Rev. Lett.* **99**, 196601 (2007).
- ²²H. Sakurai, *Phys. Rev. B* **78**, 094410 (2008).
- ²³T. Qian, K. Nakayama, Y. Sun, T. Arakane, T. Sato, T. Takahashi, K. Yamaura, and E. Takayama-Muromachi, *J. Phys. Soc. Jpn.* **78**, 024709 (2009).
- ²⁴J. Sugiyama, Y. Ikedo, T. Goko, E. J. Ansaldo, J. H. Brewer, P. L. Russo, K. H. Chow, and H. Sakurai, *Phys. Rev. B* **78**, 224406 (2008).
- ²⁵O. Ofer, Y. Ikedo, T. Goko, M. Mansson, J. Sugiyama, E. J. Ansaldo, J. H. Brewer, K. H. Chow, and H. Sakurai, *Phys. Rev. B* **82**, 094410 (2010).
- ²⁶H. Nozaki, J. Sugiyama, M. Mansson, M. Harada, V. Pomjakushin, V. Sikolenko, A. Cervellino, B. Roessli, and H. Sakurai, *Phys. Rev. B* **81**, 100410 (2010).
- ²⁷*International Table for Crystallography*, edited by Th. Hahn (Kluwer Academic, Dordrecht, 2002), Vol. A.
- ²⁸G. M. Volkoff, H. E. Petch, and D. W. Smellie, *Can. J. Phys.* **30**, 270 (1952).
- ²⁹M. Itoh, I. Yamauchi, T. Kozuka, T. Suzuki, T. Yamauchi, J. I. Yamaura, and Y. Ueda, *Phys. Rev. B* **74**, 054434 (2006).
- ³⁰T. Suzuki, I. Yamauchi, M. Itoh, T. Yamauchi, and Y. Ueda, *Phys. Rev. B* **73**, 224421 (2006).
- ³¹*Atomic and Molecular Physics*, edited by K. H. Hellwege and A. M. Hellwege, Landolt-Bornstein, New Series, Group II (Springer, Berlin, 1986), Vol. 16.
- ³²Y. Yafet and V. Jaccarino, *Phys. Rev. A* **113**, 1630 (1964).
- ³³A. Abragam and F. Bleaney, *Electron Paramagnetic Resonance of Transition Ions* (Clarendon, Oxford, 1970).
- ³⁴K. Takanashi, H. Yasuoka, Y. Ueda, and K. Kosuge, *J. Phys. Soc. Jpn.* **52**, 3953 (1983).
- ³⁵E. D. Jones, *Phys. Rev. A* **137**, 978 (1965).
- ³⁶T. Ohama, H. Yasuoka, M. Isobe, and Y. Ueda, *J. Phys. Soc. Jpn.* **66**, 3008 (1997).
- ³⁷Y. Shimizu, K. Matsudaira, M. Itoh, T. Kajita, and T. Katsufuji, *Phys. Rev. B* **84**, 064421 (2011).
- ³⁸T. Kiyama and M. Itoh, *Phys. Rev. Lett.* **91**, 167202 (2003).
- ³⁹W. G. Clark, M. E. Hanson, W. H. Wong, and B. Alavi, *J. Phys. IV* **3**, C2-235 (1993).
- ⁴⁰R. Bursill, G. A. Gehring, D. J. J. Farnell, J. B. Parkinson, T. Xiang, and C. Zeng, *J. Phys.: Condens. Matter* **7**, 8605 (1995).
- ⁴¹B. J. Gibson, R. K. Kremer, A. V. Prokofiev, W. Assmus, and G. J. McIntyre, *Physica B* **350**, 253 (2004).
- ⁴²M. Enderle, C. Mukherjee, B. Fak, R. K. Kremer, J.-M. Broto, H. Rosner, S.-L. Drechsler, J. Richter, J. Malek, A. Prokofiev, W. Assmus, S. Pujol, J.-L. Raggazzoni, H. Rakoto, M. Rheinstadter, and H. M. Ronnow, *Europhys. Lett.* **70**, 237 (2005).
- ⁴³N. Buttgen, H.-A. Krug von Nidda, L. E. Svistov, L. A. Prozorova, A. Prokofiev, and W. Assmus, *Phys. Rev. B* **76**, 014440 (2007).
- ⁴⁴S.-L. Drechsler, O. Volkova, A. N. Vasiliev, N. Tristan, J. Richter, M. Schmitt, H. Rosner, J. Malek, R. Klingeler, A. A. Zvyagin, and B. Buchner, *Phys. Rev. Lett.* **98**, 077202 (2007).